THE ASTROPHYSICAL JOURNAL, 414:219–229, 1993 September 1

HIGH-RESOLUTION X-RAY SPECTROSCOPY OF THE SUPERNOVA REMNANT N132D

UNA HWANG,[1] JOHN P. HUGHES,[2] CLAUDE R. CANIZARES,[1] AND THOMAS H. MARKERT[1]
Received 1992 December 18; accepted 1993 March 10

ABSTRACT

We present a joint nonequilibrium ionization analysis of spectral data from the *Einstein Observatory* of the supernova remnant N132D in the Large Magellanic Cloud. We use high spectral resolution data from the Focal Plane Crystal Spectrometer (FPCS) and the Solid State Spectrometer (SSS), and lower spectral resolution data from the Imaging Proportional Counter (IPC) and Monitor Proportional Counter (MPC). Our updated analysis uses new calibrations for the FPCS and SSS efficiencies and a single-temperature, single-ionization time-scale model for the plasma. The FPCS detected individual emission lines of O VII, O VIII, Ne IX, Ne X, Fe XVII, and possibly Fe XX. Measured line widths for the oxygen lines suggest Doppler broadening that is roughly consistent with optically measured expansion velocities of 2250 km s^{-1}. Constraints on temperature and ionization age from measured FPCS line flux ratios are consistent with results of spectral fits to the SSS and IPC data, which give a temperature of 8.4 $(+0.8; -0.6) \times 10^6$ K and an ionization age of 6.1 $(+5.0; -2.6) \times 10^3$ cm^{-3} yr. At the SSS/IPC temperature, FPCS flux ratios constrain the O/Fe abundance to be at least 1.9 times its solar value and the O/Ne abundance to be 0.2–1.0 times its solar value. The SSS/IPC fits provide constraints of 1.0–4.0 times solar for O/Fe and 0.5–1.5 times solar for O/Ne which are consistent with the FPCS results. We are puzzled to find that the SSS/IPC fits indicate abundances of oxygen and other heavy elements relative to the light elements that are below both their solar values and their mean values for the LMC. We therefore compare abundance ratios to calculations for the composition of ejecta from Type II supernovae including a contribution from swept-up interstellar material with elemental abundances appropriate for the LMC. Models for remnants with progenitor masses of 20 and 25 $M_\odot$ are completely consistent with the data, while remnants with progenitor masses of 13 and 15 $M_\odot$ can be made consistent if the progenitors are required to eject a large fraction of their iron cores.

Subject headings: ISM: individual (LMC N132D) — Magellanic Clouds — supernova remnants — X-rays: interstellar

1. INTRODUCTION

Supernova remnant N132D in the Large Magellanic Cloud (LMC) was identified as a nonthermal radio source by Westerlund & Mathewson in 1966. Since then, optical observations have placed N132D in a class of remnants, typified by Cassiopeia A in our galaxy, which have large expansion velocities (≥ 1000 km s^{-1}) and are rich in oxygen emission. Observations by Danziger & Dennefeld (1976) and Lasker (1978) show that N132D has a complex spatial structure in the optical that can be divided into the following: a ring of oxygen-rich filaments expanding at large velocities, a relatively quiescent outer shell, and an extended region of diffuse material. Individual oxygen-rich filaments in the ring have masses of $\simeq 0.0015\ M_\odot$ and O/H abundance ratios enhanced 10–100 times relative to the LMC remnant N49. Expansion velocities for the oxygen ring give an age assuming free expansion of approximately 1300 yr for the remnant (Lasker 1980).

X-ray observations of N132D were carried out between 1979 and 1981 by the *Einstein Observatory*. The X-ray image from the High Resolution Imager (HRI; Hughes 1987) shows an X-ray structure similar to the optical structure with the exception that the large region of diffuse emission is absent. A radius of $\simeq 44''$ (corresponding to 11.7 pc at a distance of 55 kpc for the Large Magellanic Cloud) was determined for the remnant from the surface brightness profile. Densities for the X-ray-emitting region were derived by normalizing model surface brightness profiles to the data. An isothermal shell model gave densities of 3–12 cm^{-3}, and the standard Sedov (1959) model gave densities of 7–12 cm^{-3}, corresponding to shock temperatures of $10^{6.8}$–$10^{7.1}$ K. For the Sedov model, these values plus the measured gas temperature and a corresponding radius of $11 \leq R(\mathrm{pc}) \leq 13$ gave an explosion energy of $2.3 \leq E(10^{51}$ ergs$) \leq 11.4$ and an age of $4300 \leq t(\mathrm{yr}) \leq 7200$. Observed variations in the surface brightness of the outer shell can be explained if the explosion occurred in a low-density cavity in the interstellar medium. The data are then qualitatively well fitted if the low-density region was an H II region surrounding a progenitor of stellar type later than B0. In addition, energy and age estimates would be lower than in the Sedov model, and agreement with Lasker's (1980) dimensional age estimate could be obtained with a cavity density of $\simeq 0.01$ cm^{-3}.

Previous spectral analyses of N132D have been performed with X-ray data obtained by the *Einstein Observatory*, with the assumption that the plasma is in collisional ionization equilibrium. Analysis of low spectral and spatial resolution data for energies 0.2–4.0 keV from the Imaging Proportional Counter (IPC) gave temperatures $T = 10^{6.8}$–$10^{7.1}$ K and hydrogen column densities $N_H = 10^{21}$–$10^{21.5}$ cm^{-2}. The unabsorbed source luminosity between 0.2 and 4.0 keV was given as $(4.5–7.5) \times 10^{37}$ ergs s^{-1} for a distance of 55 kpc for the LMC (Hughes 1987). Thermal bremsstrahlung fits to data from the Monitor Proportional Counter (MPC) gave $T = 10^{6.9}$ K and $N_H = 10^{21.3}$ cm^{-2}. Higher spectral resolution data for energies between 0.4 and 4.0 keV taken with the Solid State Spectrometer (SSS) required a two temperature collisional ionization

[1] Center for Space Research and Department of Physics, Massachusetts Institute of Technology, 70 Vassar Street, Cambridge, MA 02139.
[2] Harvard-Smithsonian Center for Astrophysics, 60 Garden Street, Cambridge, MA 02138.

equilibrium model for an adequate fit with $T_{\rm lower} = 10^{6.82}$ and $T_{\rm upper} = 10^{7.67}$; $N_{\rm H}$ was given as $10^{20.76}$–$10^{21.1}$ cm^{-2} for the lower temperature component (Clark et al. 1982). Clark et al. suggest that a two-temperature model is required because the plasma is not in collisional ionization equilibrium.

Here we present the first nonequilibrium collisional ionization analysis of all the X-ray spectral data obtained by the *Einstein Observatory* for N132D. We report new results for high spectral resolution data obtained by the Focal Plane Crystal Spectrometer (FPCS), which detected individual emission lines of O VII, O VIII, Ne IX, Ne X, Fe XVII, and possibly Fe XX, and by the SSS. We also present lower spectral resolution data from the IPC and MPC. We use a simple two-parameter model in which the emission from a plasma not in collisional ionization equilibrium is characterized by a global temperature and a global ionization age. Ratios of line fluxes measured by the FPCS are used to constrain the temperature, ionization age, and relative elemental abundances in the plasma. The SSS and IPC spectrum is fitted to this model to estimate the temperature, ionization age, column density, and elemental abundances. Results from the two data sets are found to be consistent. A preliminary analysis of the FPCS data was presented by Canizares et al. (1983), Markert et al. (1984), and Canizares (1985, 1990a). More refined analysis was made possible by improved spatial resolution using the HRI X-ray image of N132D (Hughes 1987) and improved detector efficiency calibrations.

2. DATA ANALYSIS

2.1. *FPCS Data*

The Focal Plane Crystal Spectrometer (FPCS) provided the highest spectral resolution observations of N132D obtained by the *Einstein Observatory* (Giacconi et al. 1979). Observations were performed on 4 days in 1979 and 1980 with a 6′ diameter circular aperture which easily accommodated N132D's small size of 90″ in its field of view. X-rays focused by the telescope passed through a selectable aperture to strike one of six curved diffractors where X-rays with wavelengths near those required by Bragg geometry were reflected by the crystal and detected by one of two proportional counters. The crystal was slowly rocked back and forth to scan a width of several spectral resolution elements centered on a feature of interest. Positions and Bragg angles were corrected for offset of the instantaneous position of the source image from the telescope axis by using satellite aspect solutions.

The detector was a position-sensitive proportional counter which provided a spatial resolution of approximately 1.5 mm FWHM in the direction of spectral dispersion, corresponding to 1.′5 on the sky. In the FPCS configuration, photons originating at different positions in the sky strike the crystal at different angles so that their measured energies depend both on the orientation of the crystal and their location in the X-ray source. This blurs the spectra of extended sources like N132D. By using the position information available from the FPCS detector, it is possible to sharpen the resulting spectrum. The HRI X-ray image of N132D (Hughes 1987) was used to determine the most likely sky location for each photon detected by the FPCS. FPCS photon energies and exposures were corrected appropriately. The correction is limited by the point spread function of the FPCS (1.5 mm FWHM) and by the extent to which the broad-band HRI image corresponds to the FPCS image, which is restricted to a very narrow energy band.

The analysis procedure (Canizares et al. 1979) was designed to achieve the lowest background levels. Data were first selected to exclude periods of Earth blockage, high particle background, and poor aspect solutions. Photons arriving with pulse heights outside an appropriate interval were then excluded. Optimum pulse height intervals were estimated for each observation from pre-flight and in-flight calibration data on the gain and energy resolution of the detector and from observations of the bright X-ray source Sco X-1 over the lifetime of the observatory (K. S. K. Lum, 1992, private communication). Relative positions of arrival of photons at the detector were offset slightly from wire to wire to compensate for gain variations and geometrical effects due to the curvature of the crystal, and photons arriving outside the region of the detector containing the source signal were then excluded. In calculating line fluxes, we corrected for source counts that may have been excluded by the cuts in pulse height and detector position by assuming a Gaussian distribution of source photons in these parameters. We also corrected for the exclusion of data from specific wires by using predictions for the number of photons at a given energy detected at each wire from a ray-tracing simulation for a point source. The total correction factor ranged from 1.1 to 1.2 for most observations. For all observations, particle background count rates were determined independently in the regions of the detector outside the source image. The FPCS scans are not well suited to determining the continuum level, so we account only for the non-X-ray particle background.

In regions where the emission lines are blends that were only partially resolved by the FPCS, we fit the observed spectrum by modeling emission lines as Gaussians and adding an independently determined, fixed background. Relative line intensities within a multiplet and all relative line energies were fixed at theoretical values, while overall line intensities and the overall energy scale were allowed to vary. The line FWHM was fixed at a width determined by the detector's spatial resolution. We used a maximum likelihood fitting algorithm and calculated Poisson probability contours for the line intensities and for line intensity ratios. Errors for each parameter were estimated by projecting two-dimensional Poisson confidence contours onto the appropriate axes.

In the region 800–840 eV, we modeled the Fe XVII triplet and the O VIII Lyγ and Lyδ lines. The relative intensities within the multiplets of iron and oxygen were set at values observed in solar flares by SOLEX (McKenzie et al. 1980), and the overall strengths of the iron and oxygen multiplets were varied separately. We used 3 eV energy bins for the data and a Gaussian FWHM of 8 eV for the fit. In the region 900–930 eV, we modeled the Ne IX triplet. The relative strengths of the intercombination and forbidden lines were held fixed at the value 0.28 from Pradhan (1982), while the overall strengths of the forbidden and resonance lines were varied. We used 5 eV energy bins and a Gaussian FWHM of 11 eV. These data and the fitted models are shown without correction for instrumental efficiency in Figure 1, while the fitted energies and fluxes are given in Table 1.

At the temperatures and ionization ages of interest for N132D, the total Fe XIX flux in the region of the Fe XVII triplet is calculated to be equal to or less than the flux in the Fe XVII line at 15.01 Å (see § 3.2 and 3.3 for discussion of these calculations). The Fe XIX flux is distributed over 24 lines, however, and not all of these fall within the FPCS scan. Since relative intensities and collision strengths were not available for these lines, we neglected wavelength-dependent factors and

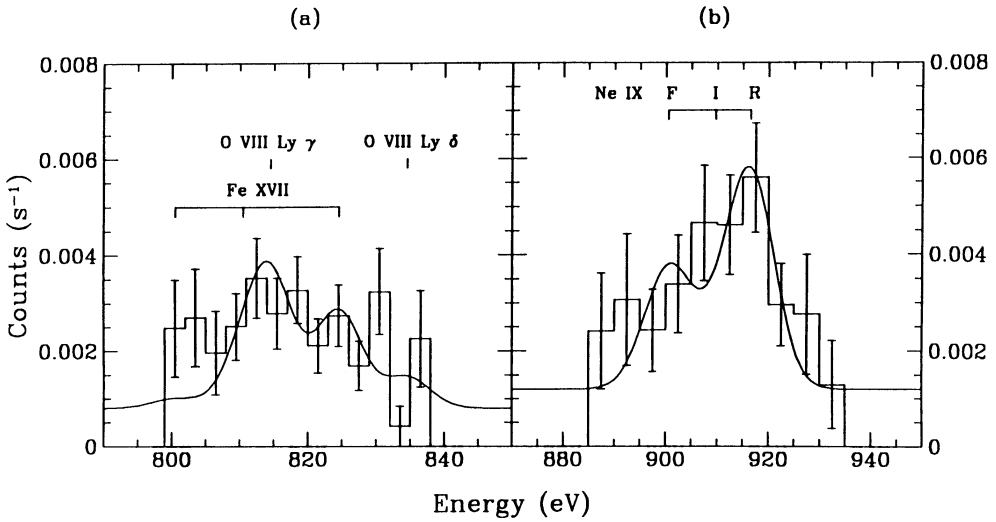

FIG. 1.—FPCS data without correction for instrumental efficiency and fitted models for emission lines in the regions 800–840 eV (*a*) and 900–935 eV (*b*). The background is fixed at an independently determined value, and the Gaussian FWHM for the emission lines is fixed at a value determined by the detector's spatial resolution. Strengths of lines in each multiplet are fixed at theoretical values.

estimated the relative strength of a line in this complex to be roughly proportional to the oscillator strength to the ground state weighted by a branching ratio. The oscillator strengths and wavelengths were taken from Bhatia et al. (1989). The strongest of the Fe XIX lines falling within the FPCS scan is blended with the Fe XVII line at 15.01 Å, but should be no more than roughly one-fourth as strong.

In the region of the Ne IX triplet, the Fe XIX lines are potentially strong enough to contaminate the data. We fit the data including the strongest Fe XIX lines in the scan, setting their relative intensities at values from Bhatia et al. The resulting best-fit Ne IX flux is reduced by a factor of about 2.5 from the value in Table 1, but the 2 σ errors for the Fe XIX and Ne IX intensities are both consistent with zero, and the quality of the fit is not significantly improved. We concluded that our data are not of sufficient quality to study reliably the iron lines in this region. In any case, our other results are not significantly changed by adopting the results of this fit.

The complete spectrum of N132D obtained by the FPCS is shown in Figure 2 corrected for instrumental efficiency but uncorrected for interstellar absorption or for cuts in pulse height and pulse position. This may be compared to the spectrum presented by Canizares et al. (1983). Line fluxes are given in Table 1, both uncorrected for absorption and a correction for absorption corresponding to $N_H = 6.25 \times 10^{20}$ cm^{-2}, our best-fit hydrogen column density from SSS and IPC data (see § 3.2). Actual detected photon numbers and estimated background photon numbers in the source region of the detector are given along with confidence levels for Poisson statistics. The identification of lines in the Fe XX and Ne X Lyβ scans is uncertain because of their relatively low fluxes and relatively large offsets from the expected line energies.

TABLE 1

FPCS LINE FLUXES

Line	Observed Energy (eV)	Rest Energy (eV)	Flux (10^{-3} photons cm^{-2} s^{-1})	Unabsorbed[a] Flux (10^{-3} photons cm^{-2} s^{-1})	Total Counts	Background Counts	CL[b]	CF[c]
O VII Res	572	574	1.85 ± 0.93	3.13 ± 1.57	15	7.1	0.993	0.50
O VIII Lyα	652	654	10.37 ± 1.26	14.98 ± 1.82	130	32.7	1.000	0.11
O VIII Lyβ	771	774	2.12 ± 0.47	2.74 ± 0.61	46	12.9	1.000	0.34
O VIII Lyγ	814	816	$1.95^{+0.70}_{-0.72}$	$2.44^{+0.88}_{-0.90}$	...	...	...	0.17
Fe XVII	824	826	$1.54^{+0.59}_{-0.60}$	$1.91^{+0.73}_{-0.74}$	...	...	...	0.17
Ne IX For	900	906	$1.99^{+0.91}_{-1.18}$	$2.42^{+1.11}_{-1.44}$	...	...	...	0.22
Ne IX Res	916	922	3.25 ± 1.25	3.95 ± 1.52	...	...	...	0.22
Ne IX Heα[d]	...	...	$5.80^{+1.71}_{-1.96}$	$7.00^{+2.06}_{-2.37}$	...	...	...	0.22
Fe XX[e]	957	967	0.56 ± 0.50	0.66 ± 0.59	16	11	0.907	0.45
Ne X Lyα	1010	1022	6.07 ± 0.89	7.00 ± 1.03	111	32.6	1.000	0.21
Ne X Lyβ	1175	1212	0.83 ± 0.23	0.91 ± 0.25	46	22.9	1.000	0.72

[a] Corrected for $N_H = 6.25 \times 10^{20}$ atoms cm^{-2}.
[b] Confidence level for detection from Poisson statistics.
[c] Continuum fraction for FPCS scan predicted by best-fit nonequilibrium ionization model for SSS/IPC data.
[d] Ne IX Heα = Ne IX Res + 1.28 Ne IX For (Pradhan 1982).
[e] Uncertain line identification.

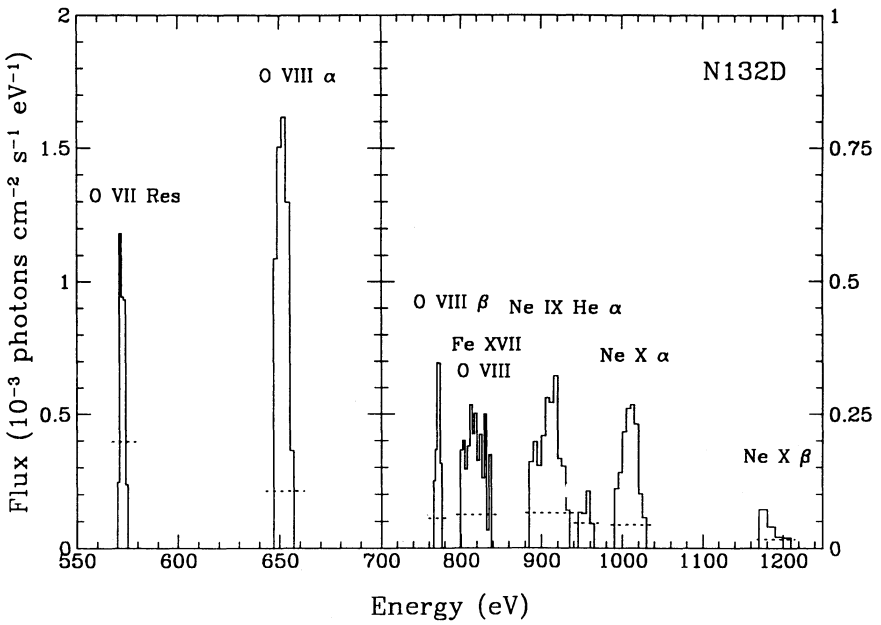

FIG. 2.—FPCS spectrum of N132D, corrected for instrumental efficiency, uncorrected for interstellar absorption. Background levels for each observation are indicated by the dotted lines. Note the change in x- and y-axes scales at an energy of 700 eV.

A significant portion of the X-ray emission from N132D is in oxygen lines, as the preliminary analysis indicated. The unabsorbed X-ray luminosity from the O VIII Lyα line alone is $(5.0 \pm 0.5) \times 10^{36}$ ergs s^{-1} for a distance of 50 kpc to the LMC, accounting for approximately 10% of the unabsorbed luminosity of 4.6×10^{37} ergs s^{-1} between 0.2 and 4.0 keV from our best-fit NEI model to the joint SSS and IPC data. (Similar values for the broad-band luminosity of N132D as estimated from the IPC data have been given by Hughes 1987: $[4.5–7.5] \times 10^{37}$ ergs s^{-1} between 0.2 and 4.0 keV, and by Long, Helfand, & Grabelsky 1981: 8.3×10^{37} ergs s^{-1} between 0.15 and 4.5 keV. These luminosities are given for an older value of the distance to the LMC of 55 kpc. We pefer the more recently determined value of 50 kpc from Panagia et al. 1991.).

We examined the widths of oxygen lines for evidence of Doppler broadening, since N132D is dominated in the optical by high-velocity oxygen lines. After fitting the data to Gaussian line profiles, the width in excess of the expected width from the spectral and spatial resolution of the detector was attributed to Doppler broadening. The 90% confidence limits for the width of the O VIII Lyα line correspond to velocities between 1000 and 2000 km s^{-1}. The 90% confidence limits for the O VIII Lyβ line rule out velocities above $\sim$3000 km s^{-1} and are consistent with zero velocities. Our data are not adequate for precise measurements of the broadening, but our estimates suggest Doppler broadening roughly consistent with optical measurement of an expansion velocity of 2250 km s^{-1} in the oxygen-rich ring (Lasker 1980).

2.2. *SSS Data*

The Solid State Spectrometer (SSS) on board the *Einstein Observatory* was a cooled Si (Li) detector with an energy resolution of about 160 eV (FWHM), roughly independent of energy. The bandwidth (0.6–4.5 keV) was limited at the low-energy end by an aluminized Parylene filter to block UV and optical radiation, a thin gold layer for electrical contact, and an undepleted Si region on the forward face of the detector. At the high-energy end the band was defined by the rapidly falling effective area of the *Einstein* high-resolution mirror due to diminished efficiency for grazing incidence reflection of X-rays at higher energies. Shortly after launch it was noticed that there was additional absorption of low-energy X-rays, which was traced to a buildup of ice on the cooled front surface of the detector. The problem was complicated by the nature of the ice buildup (clumpy) and its time variability (an e-folding time of 0.25 day for ice buildup after defrosting; Holt et al. 1979; Christian 1992). A recent recalibration of the SSS (N. White, 1992, private communication) used observations of the Crab nebula to refine both the model for the ice buildup and the overall efficiency of the SSS.

The SSS observed N132D on 1979 September 18 (day 261) for an effective exposure time of 5900 s at a counting rate of 2.64 ± 0.02 s^{-1} for energies 0.6–4.5 keV. During the observation the amount of ice on the detector was low and stable, while the reliability in the model for the ice correction was high due to extensive observations of the Crab Nebula during this part of the mission (see below). At 0.6 keV the X-ray transmission through the ice layer estimated from the model for the N132D observations is 0.52 ± 0.07. Our derived best-fit column density to N132D (see below) is $(6.25[+2.16; -1.77]) \times 10^{20}$ cm^{-2}, which corresponds to a transmission of only 0.63 ± 0.09 at 0.6 keV. We conclude that the fractional error in the column density to the source is dominated by the statistical uncertainty in the fits and not by the systematic uncertainty in the ice model.

We extracted the SSS data, response functions, and correction spectrum from the *EXOSAT* database. All data were converted to ASCII format and ported to a local machine where they were integrated into the NEI model fitting software. In order to verify our data extraction procedure and analysis software, we also extracted the data from three SSS observations of the Crab Nebula closest in time to the N132D observation. These were the observations from days 260, 261, and 263 of year 1979. The Crab data were processed in exactly the same

manner as were the N132D data. Fits to these data of an absorbed power law yielded best-fit values of 9.41, 9.99, and 10.28 for the normalization; 2.084, 2.126, and 2.169 for the spectral index α; and 21.549, 21.540, and 21.561 for log N_H. These compare quite well with the values derived from fitting the FPCS data of the Crab Nebula (Schattenburg & Canizares 1986): a normalization of 10.9 ± 1.4, a spectral index α of 2.1 (fixed), and a column density of 21.54 ± 0.05. This comparison verfies our analysis procedure for the SSS data, checks the ice correction model, and establishes consistency between the SSS and the FPCS data sets.

2.3. *IPC Data*

The *Einstein* Imaging Proportional Counter (IPC) was a low-background gas-filled detector with modest imaging and some spectral capabilities. Due to the small angular size of N132D (about 90″), the IPC was unable to yield spatially resolved spectra. Our global spectrum was extracted from field I2448 observed (on 1979 April 12) for a dead-time corrected exposure time of 1240 s. The source was 4′.7 off-axis. We integrated the IPC counts within a 3′ circle centered on the source position and estimated the background from a 4′–6′ annular region. The count rate was $3.98 \pm 0.06\ s^{-1}$ over the band 0.2–4.0 keV. For the spectral analysis, in each pulse height bin a 3% systematic error was added in quadrature with the statistical error to account principally for uncertainty in the spectral calibration of the IPC. The gain of the detector was estimated based on the average gain of the field (BAL = 12.61) and the position of N132D in detector coordinates.

As we show below, the IPC and SSS data are consistent with each other for the simple (single temperature–single time scale) nonequilibrium ionization (NEI) model we introduce here. This agreement gives further confidence in the reliability of the ice correction for the SSS and the gain and efficiency calibration of the IPC. We note, however, that we must introduce a relative normalization between the SSS and IPC of about 0.8 (SSS/IPC). This may be due to residual uncertainties in the calibration of the overall effective areas of the two instruments since accurate in-flight calibration of the IPC effective area using the Crab Nebula was corrupted by the necessarily large dead-time corrections required.

2.4. *MPC Data*

For completeness we have examined the *Einstein* Monitor Proportional Counter (MPC) data for this source. The MPC was a nonimaging proportional counter (energy band 2–10 keV) with a geometric collecting area of 667 cm^2 that was co-aligned with the *Einstein* telescope. There was an MPC spectrum taken with each observation done by the *Einstein Observatory*. Although the total exposure time on N132D was quite large (over 80,000 s) the MPC spectra are dominated by systematic errors in the calibration and background subtraction. The field of view was mechanically collimated to a roughly 45′ square region of the sky. This fact, in addition to the large systematic errors, severely limits the usefulness of the MPC data particularly for N132D which lies in a source-rich region of the LMC.

The MPC spectra are inconsistent with the best-fit single-temperature NEI model for the combined SSS and IPC data. The joint fit of the SSS, IPC, and MPC data can be improved significantly by including a second slightly harder thermal component ($kT \sim 2.0$ keV) with an emission measure only 5.8% of the main component ($kT \sim 0.6$ keV, see below). In comparing this new model to the single-temperature one, we find that the temperature of the main component drops slightly (about 7%), and the ionization age and column density remain about the same. The fitted abundance of oxygen also remains nearly the same, while the abundances of elements beyond oxygen all increase somewhat; for example, neon and iron increase by 60% and 25%, respectively.

Although the existence of a harder spectral component in the MPC data is strongly indicated, we seriously question whether the current data support N132D as the origin of this emission. Diffuse emission from the LMC or an unrelated object in the large field of view of the MPC could just as easily be the source. The issue of the presence of a second thermal component in N132D has important consequences in light of its complex morphology and models for the origin of this structure (Hughes 1987). However, we must leave a definitive answer to this question to future broad-band X-ray observations. In the remainder of this paper we consider only the IPC and SSS data and a single-temperature NEI model.

3. RESULTS

3.1. *Nonequilibrium Ionization*

Previous X-ray spectral studies of N132D have used collisional ionization equilibrium (CIE) models for the emitting plasma (Clark et al. 1982; Hughes 1987). However, supernova remnants are not expected to be in ionization equilibrium. As pointed out by Gorenstein, Harnden, & Tucker (1974), the time scale for this equilibrium is typically $\sim 2 \times 10^4/n_e$ yr, where n_e(in cm^{-3}) is the electron density of the plasma. For low-density plasmas like supernova remnants, which have $0.1 \leq n_e\ (cm^{-3}) \leq 100$, this equilibrium time often exceeds the known or deduced age of the remnant. Plasma diagnostics like the ones we use for the FPCS data have established that many supernova remnants are in fact not in ionization equilibrium. Examples include Puppis A (Canizares et al. 1983; Winkler, Canizares, & Bromley 1983) and the 20,000 year old Cygnus Loop (Vedder et al. 1986; see also Canizares 1985, 1990b for reviews).

Nonequilibrium effects have been incorporated into detailed models of supernova remnants by several authors, including Itoh (1977), Gronenschild & Mewe (1982), Shull (1982), Hamilton, Sarazin, & Chevalier (1983), Nugent (1984), and Hughes & Helfand (1985). Their approach has been to combine the nonequilibrium ionization structure with either numeric or analytic (Sedov 1959) solutions for the hydrodynamics of a spherically symmetric blast wave propagating through a homogeneous medium. We may, however, describe the bulk characteristics of the emergent spectrum simply with a global temperature T and a global ionization age $\tau \equiv \langle \int n_e(t)dt \rangle$, where n_e is the post-shock electron density of a parcel of gas in the remnant, the integration is carried out from the time the gas is shocked to the present, and an average calculated for all the gas in the remnant (Hamilton & Sarazin 1984). In this simple two-parameter model, elemental abundances may be estimated once τ and T are constrained.

3.2. *SSS and IPC Analysis*

Our spectral model for the SSS and IPC broad-band data coupled a nonequilibrium ionization calculation with the plasma emission code of Raymond & Smith (1977; 1992 July 27 version). The ionization calculation was based on the matrix solution developed by Hughes & Helfand (1985), although the

actual code to perform the diagonalization and determine the eigenvectors has been completely rewritten since then to improve the accuracy and increase the robustness of the solution. The complement of emission lines in the Raymond & Smith code was supplemented by a number of lines from Mewe & Gronenschild (1981) which were appropriate to the NEI situation. In particular we found it necessary to include Kα transitions from low-ionization states of the astrophysically abundant elements as well as emission from innershell ionization processes. The model also includes continuum emission from all elemental species considered by bremsstrahlung, radiative recombination, and two photon processes. For computational reasons we precomputed a large grid of models in the $\tau - T$ plane, keeping the emission from the astrophysically abundant elements (H, He, C, N, O, Ne, Mg, Si, S, Ar, Ca, Fe, and Ni) separate in order to allow subsequent adjustment of the elemental abundances. We developed a scheme which eliminates the problem of choosing a model grid, which arises in the joint analysis of multi-mission broad-band X-ray data. Usually, a fine binning in energy is used in the precomputed model and then interpolated for the various energy binnings required by the various instruments. This tends to smear sharp lines into several bins. Our solution was to store the emission lines separately from the continuum. The continuum, which varies smoothly with energy, can be interpolated rather accurately onto the various grids corresponding to different instruments. At this point in the fitting routine the emission lines are put into the proper energy bins as well.

When fitting the NEI model to broad-band X-ray spectral data for N132D, the electron temperature is determined by the shape of the continuum emission, the ionization age is determined by the centroid energies of the various K-shell lines (which are, after all, blends of lines from hydrogen-like ions, and so on), and the elemental abundances are determined from the relative intensities of the lines. Absorption due to material along the line of sight according to Morrison & McCammon (1983) was incorporated into the model fits.

The SSS and IPC data are shown in Figure 3 (uncorrected for instrumental response) along with the best-fit model. Table 2 summarizes the best-fit parameters and 90% single parameter confidence errors of the model. The fit of a single-temperature, single-time-scale NEI model to the joint SSS and IPC is acceptable (the confidence level for rejecting the model based on the best-fit χ^2 value is 20%). The temperature was constrained, largely by the shape of the continuum, to be log T(K) = 6.93 (+0.04; −0.03), and the hydrogen column density was found to be log $N_{\rm H}$(cm^{-2}) = 20.80 (+0.12; −0.15). The ionization age log τ(cm^{-3} yr) = 3.78 (+0.26; −0.24) was sensitive mostly to the line centroids of the Mg, Si, and S line blends. From these fits we can reject a value of τ greater than $10^{4.5}$ cm^{-3} yr at more than 3 σ, which confidently establishes that this remnant, like the Cygnus Loop and Puppis A, is still in the ionizing phase in the evolution of its global X-ray spectrum.

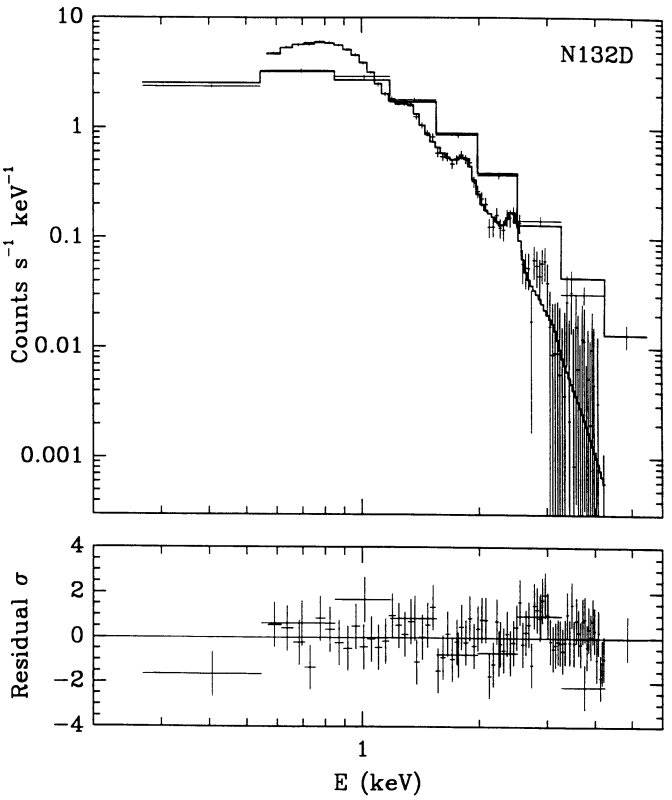

FIG. 3.—SSS and IPC spectra of N132D, uncorrected for instrumental efficiencies, together with the best-fit single-temperature, single ionization age nonequilibrium ionization model. We are unwilling to ascribe a physical interpretation to the bump in the residuals around 2.9 keV in the SSS data. The presence in the detector of a temporally variable background in this energy range makes accurate modeling difficult.

TABLE 2

BEST-FIT PARAMETERS FOR SSS/IPC ANALYSIS: NEI MODEL

Parameter	Best-Fit Value[a]	LMC Mean Value[b]
T (K)	$8.4^{+0.8}_{-0.6} \times 10^6$	...
$n_e t$ (cm^{-3} yr)	$6.1^{+5.0}_{-2.6} \times 10^3$	...
$N_{\rm H}$ (atoms cm^{-2})	$6.25^{+2.16}_{-1.77} \times 10^{20}$	...
Emission integral ($n_{\rm H}^2 V$)[c] (cm^{-3})	$5.72^{+0.52}_{-0.47} \times 10^{60}$	...
(O/H)/(O/H)$_\odot$	$0.205^{+0.043}_{-0.037}$	$0.339^{+0.050}_{-0.044}$
(Ne/H)/(Ne/H)$_\odot$	$0.230^{+0.049}_{-0.044}$	$0.490^{+0.060}_{-0.053}$
(Mg/H)/(Mg/H)$_\odot$	$0.250^{+0.071}_{-0.064}$	$1.122^{+0.392}_{-0.290}$
(Si/H)/(Si/H)$_\odot$	$0.191^{+0.052}_{-0.048}$	1.950
(S/H)/(S/H)$_\odot$	$0.40^{+0.13}_{-0.12}$	$0.316^{+0.073}_{-0.059}$
(Ar/H)/(Ar/H)$_\odot$	$0.10^{+0.58}_{-0.10}$	$0.246^{+0.191}_{-0.107}$
(Fe/H)/(Fe/H)$_\odot$	$0.107^{+0.0091}_{-0.0081}$	$0.427^{+0.162}_{-0.118}$
χ^2 (d.o.f.)	65.33 (76)	...

[a] Statistical errors at 90% confidence.
[b] Russell & Dopita 1992; 1 σ scatter in measurements.
[c] Assumes 50 kpc distance, $n_e/n_{\rm H} = 1.178$.

The fit was optimized for the case where the elements He, C, and N were fixed at their solar abundances relative to H (Allen 1973; we use these values for the solar abundance throughout this paper), and the remaining elements were allowed to be free. The fitted abundance values we obtained are listed in Table 2 relative to their solar values, and compared to average abundances for the Large Magellanic Cloud from Russell & Dopita (1992). In general, the abundances required for N132D are low, both relative to solar values and to the low-metallicity gas in the Large Magellanic Cloud. The errors given for the abundances are 90% confidence statistical errors at the best-fit values of $N_{\rm H}$, τ, and T. The effect of varying these three global spectral parameters on the elemental abundances is shown in Figure 4, which shows one-dimensional χ^2 curves for $N_{\rm H}$, τ, and T, and illustrates the variation of the best-fit elemental

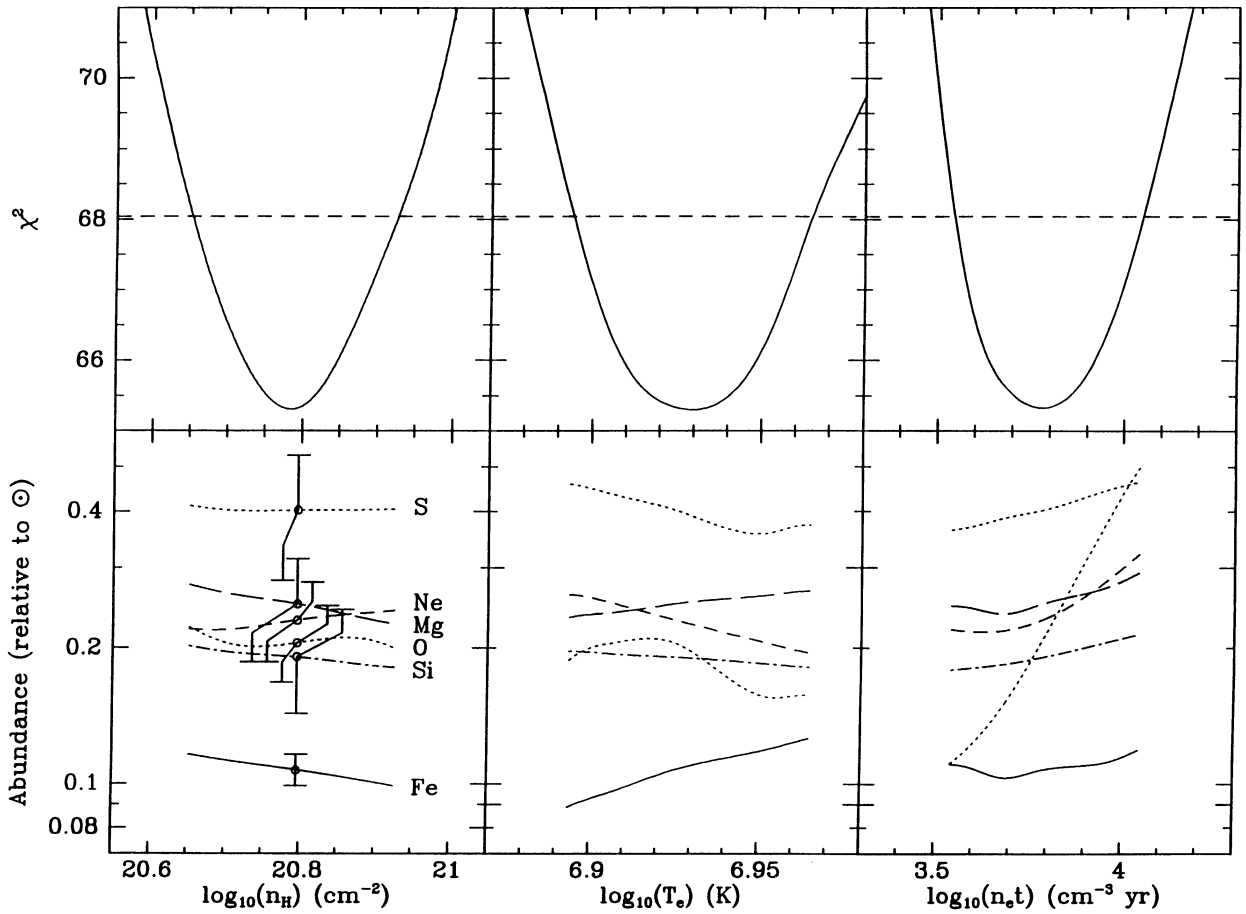

FIG. 4.—Effect of variation in column density N_H, temperature T, and ionization age τ on the best-fit elemental abundances from SSS/IPC data. For each of the three vertical segments, the upper panel shows the variation in χ^2 with the independent variation of the relevant parameter between its 90% confidence limits, while the lower panel shows the variation of the elemental abundances. The error bars show the 90% confidence statistical errors for the abundances at the best fit.

abundances with the independent variation of these parameters within their 90% confidence limits. In some cases the systematic errors on the abundance are larger than or comparable to the statistical error. The factor of 4 variation in the oxygen abundance as the ionization age increases is the extreme example. Note that the data were quite insensitive to the actual abundances of He, C, and N relative to H, since none of these elements produce significant emission lines within the SSS energy band. For completeness we explored the following additional cases (where H and He were present, He/H was at its solar value): (1) C, N, and O abundances varied together in relative proportions given by their solar ratios; (2) C, N, and O abundances all varied freely; (3) C and N absent; and (4) H and He absent. None of these cases resulted in a significant change in the χ^2 value when compared to the best-fit case. For cases (1), (2), and (3), the inferred abundances of elements from O to Fe remained less than solar, although the actual numerical values changed somewhat from case to case. For case (4), the elemental abundances defined relative to hydrogen were indeterminate. The fits required that the ratio of C to O be nearly 100 times the solar value and the ratio of N to O be 15 times the solar value. Nevertheless, the ratios of the heavy elements (Ne to Fe) to O were all similar to the previous cases.

It is puzzling that the fitted abundances are below their mean values for the LMC. Our tests indicate that anomalies in the abundances of light elements (specifically, abundances of C and/or N that are much greater than their solar values) could increase the derived abundances of the heavy elements. It is also possible that there is a nonthermal continuum component that we have not considered. It should be kept in mind that while the actual abundances for individual elements are sensitive to these effects, our studies have shown that the relative abundances are much less so. In all subsequent analysis, we use only the relative abundances of the elements.

Although the best-fit abundances are low relative to solar values, the cumulative energy flux shows that approximately 5.9% of the X-ray emission (0.2–4.0 keV) is coming from the O VIII Lyα line at 654 eV (from SSS/IPC alone). This is in agreement with the FPCS result and confirms the oxygen lines are dominating the X-ray emission from N132D.

For comparison to FPCS results below, we note that the abundance of oxygen relative to iron is enhanced 1.92 (+0.36; −0.32) times over its solar value, the abundance of neon relative to iron is enhanced 2.15 (+0.46; −0.41) times its solar value, and the abundance of oxygen relative to neon is 0.89 (+0.30; −0.22) times its solar value, where the errors are 90% confidence limits from the statistical errors at the best fit. The errors here are calculated from the fitted emission measures for each element (not from the results in Table 2) in order to avoid including the error in the overall emission measure which clearly cancels out for the abundance ratio. The range of rela-

tive abundances is somewhat larger when systematic uncertainties in the ionization age τ and temperature T are taken into account. The abundance of oxygen relative to iron is enhanced 1.0 to 4.1 times over its solar value, and the abundance of oxygen relative to neon is enhanced 0.5–1.5 times its solar value for variation of τ within its 90% confidence limits, while the abundance of neon relative to iron is enhanced 1.6–3.0 times its solar value from the variation of T within its 90% confidence limits.

3.3. *FPCS Analysis*

Model emissivity ratios were calculated for pairs of lines and line blends observed by the FPCS for a range of temperatures T and ionization times τ. The ionization structure at a given temperature and ionization age was calculated with the code of Hughes & Helfand (1985) and coupled to rate coefficients for line emission from Mewe, Gronenschild, & van den Oord (1985) and Mewe & Gronenschild (1981). Solar abundances were assumed.

Useful diagnostics can be identified by considering the expression for the flux of an X-ray line i in an ionization state z of the element $\mathscr{X}$:

$$F^i_{\mathscr{X},z} = \frac{1}{4\pi d^2}\int n_e^2 \frac{n_z(\tau)}{n_{\mathscr{X}}}\frac{n_{\mathscr{X}}}{n_{\rm H}}\epsilon_i(T)e^{-E/kT}e^{\sigma(E)N_{\rm H}}dV\ ,$$

where d is the distance to the source, n_e is the ambient electron density, $n_z/n_{\mathscr{X}}$ is the ionization fraction of the ionization species responsible for the line, $n_{\mathscr{X}}/n_{\rm H}$ is the abundance of the element in question relative to hydrogen, σ, a function of energy E, is the cross section for interstellar absorption of hydrogen, ϵ_i, a function of temperature, is the intrinsic emissivity of the line, and the integration is over the volume of the emitting region. Note that the dependence on the ionization age τ is contained only in the ionization fraction. It is apparent that flux ratios of ions of the same element constrain the ionization age τ and the temperature T jointly, but independently of the elemental abundances. With estimates for τ and T, flux ratios of lines of similar energy in different elements constrain ratios of elemental abundances relative to the solar abundances assumed. Dependence on column density can be reduced by using lines that are relatively close in energy.

TABLE 3

FPCS Line Flux Ratios

Ratio of Corrected Fluxes	Best Value	3 σ LL	2 σ LL	2 σ UL	3 σ UL
O VIII Res/O VIII Lyα	0.21	0.05	0.09	0.36	0.45
O VIII Lyβ/O VIII Lyα.....	0.18	0.10	0.13	0.25	0.30
O VIII Lyγ/O VIII Lyβ.....	0.89	0.37	0.47	1.57	2.00
O VIII Lyγ/O VIII Lyα	0.16	0.08	0.09	0.25	0.30
Ne IX For/Ne IX Res	0.62	0	0	4.3	5.4
Ne IX Heα/Ne X Lyα	1.00	0.41	0.62	1.57	1.86
Fe XX/Fe XVII	0.35	0	0.03	1.06	1.75
Ne IX Heα/O VIII Lyα.....	0.47	0.20	0.29	0.71	0.83
Ne X Lyα/O VIII Lyα.....	0.47	0.31	0.36	0.61	0.70
Fe XVII/Ne IX Heα.....	0.27	0.09	0.13	0.54	0.85
Fe XVII/Ne X Lyα	0.27	0.10	0.15	0.44	0.54
Fe XVII/O VIII Lyγ.....	0.78	0.03	0.22	2.22	3.53
Fe XVII/O VIII Lyβ	0.70	0.24	0.35	1.25	1.61
Fe XVII/O VIII Lyα	0.13	0.05	0.07	0.20	0.24

Various FPCS flux ratios and their 2 and 3 σ limits are presented in Table 3. For intensity ratios which were determined by fits to the data as described in § 2.1, we use the corresponding Poisson confidence limits. These limits were used for comparison with model flux ratio calculations over $\tau - T$ parameter space.

Among ratios of lines of the same element, the tightest constraints on τ and T come from the O VII Res/O VIII Lyα and Ne IX Heα/Ne X Lyα flux ratios. The first two panels of Figure 5 show the regions of parameter space allowed by 2 and 3 σ limits on each flux ratio, while the last shows their intersection at the 3 σ level. The 90% confidence SSS/IPC error bars are also shown in the figure. The regions allowed by the FPCS data are compatible with each other and with the SSS/IPC results at roughly the 2 σ level. The region allowed by the Fe XX/Fe XVII ratio is also consistent with the SSS/IPC values and excludes log $T(\mathrm{K}) > 7.1$, but our line identification is uncertain so it is difficult to determine which lines in the blend to include in the calculation. The O VIII Lyβ/O VIII Lyα ratio, although somewhat high, is consistent with the other data at the 3 σ level. Ratios of O VIII Lyγ relative to O VIII Lyα and O VIII Lyβ, however, are too high for consistency. We attribute the discrepancy to unknown systematic uncertainties in the

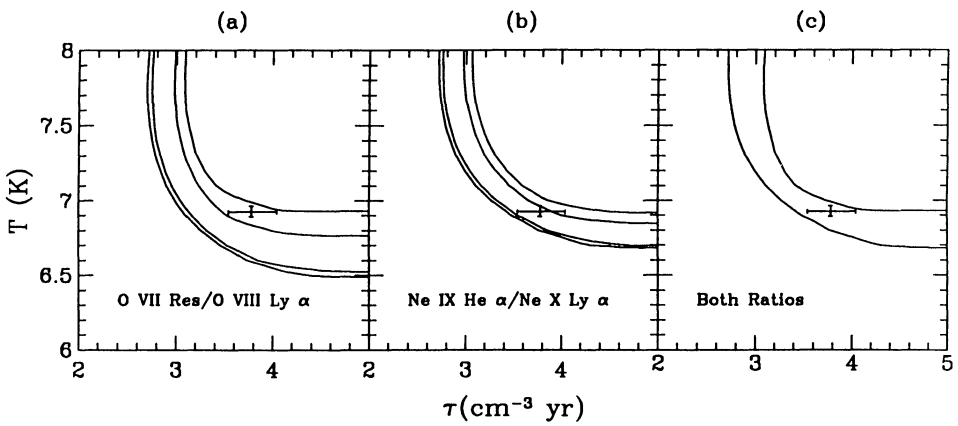

FIG. 5.—Constraints on ionization age τ and temperature T from observed 2 and 3 σ FPCS flux limits. The first panel shows constraints from O VII Res/O VIII Lyα, the second from Ne IX Heα/Ne X Lyα, and the third shows their intersection. The contours trace the locus of points with predicted flux ratios equal to each of the limits. In the first two panels, the lower flux ratio is predicted at higher values of T for a given value of τ. The error bars are the 90% confidence limits on T and τ from fits to SSS and IPC data.

efficiency of the FPCS in the vicinity of the O VIII Lyγ line. We expect that the relative fluxes of the Fe XVII and O VIII Lyγ lines will still be reliable since they were observed in the same scan and the efficiency changes slowly between 800 and 830 eV.

At this point, we adopt the SSS/IPC values for τ and T and examine ratios of lines of different elements to constrain relative elemental abundances. To estimate the relative abundance of O/Fe, we use the observed limits on the Fe XVII/O VIII Lyγ flux ratio. Since these lines were observed in the same scan, we expect their relative fluxes to be independent of the column density and relatively free of systematic uncertainties in the efficiency. In Figure 6 we show by the heavily shaded region the flux ratios predicted for solar abundances at temperatures and ionization ages within the region of $\tau - T$ space jointly allowed by the contours shown in Figure 5*c*. Only the temperature T is labeled in the abscissa in Figure 6, but the ionization age τ is related to T according to Figure 5*c*. The observed 2 σ FPCS flux limits are indicated by the lightly shaded region. Overlap of the predicted and observed ratios occurs only for log T(K) $\geq$ 7.05, but this region is inconsistent with the results of the SSS/IPC fits. For agreement of the predicted and observed ratios within the SSS error bars for T, the predicted fluxes must be decreased by a factor greater than 1.9, and perhaps by as much as an order of magnitude. The simplest

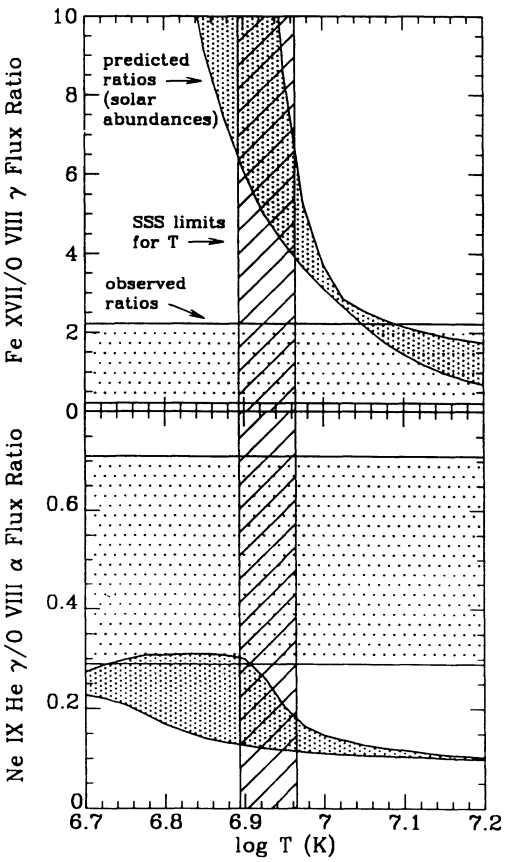

FIG. 6.—Predicted flux ratios for Fe XVII/O VIII Lyγ and Ne IX Heα/O VIII Lyα at values of temperature T and ionization age τ allowed by the FPCS data. The abscissa is labeled only by the temperature, but the ionization age is changing according to the locus of Fig. 5*c*. At a temperature of log T(K) = 6.7, log τ (cm^{-3} yr) ranges from 4.3 to 5.0, and at a temperature of log T = 7.2, log τ ranges from 3.0 to 3.25. The observed 2 σ FPCS limits are indicated by the lightly shaded region.

conclusion that can be drawn from this result is that the required enhancement of the flux ratio corresponds to an enhancement of the abundance of oxygen relative to iron compared to the solar values assumed. This is consistent with the spectral fits of the SSS and IPC, which indicate that oxygen is overabundant relative to iron by a factor of 1.0–4.1 relative to solar values as described above.

Estimates of other abundance ratios are subject to dependence on the column density, possible uncertainties in the calibration of the two FPCS detectors, and uncertainty in the true continuum level. Keeping these uncertainties in mind, we followed the procedure described above to estimate the relative abundance of O/Ne and Ne/Fe. From the ratios of Ne IX Heα and Ne X Lyα to O VIII Lyα (and O VIII Lyβ), the O/Ne abundance appears to be 0.2–1.0 times its solar value. From ratios of Fe XVII to the neon lines, the Ne/Fe abundance appears to be at least 1.2 times its solar value. Clearly, if the Fe XVII flux is overestimated because of the uncertainty in the efficiency (see above), the overabundance of Ne relative to Fe increases. These results compare well with the SSS/IPC results which give O/Ne as 0.5–1.5 times its solar value and Ne/Fe as 1.6–3.0 times its solar value.

Finally, we compared FPCS flux ratios for N132D with nonequilibrium ionization calculations for a Sedov remnant by Hamilton et al. (1983, hereafter HSC). While a region of their parameter space is allowed by our data without adjustment of elemental abundances, its temperature is too high for consistency with the SSS/IPC fits. HSC compute flux ratios over η and T_s space, where $\eta = n_0^2 E$, n_0 is the ambient interstellar hydrogen density, E is the Sedov explosion energy, and T_s is the shock temperature. Solar abundances and electron-ion equipartition were assumed. Using 2 σ limits on FPCS flux ratios of Ne IX Heα/Ne X Lyα, Fe XVII/O VIII Lyβ,[3] and Fe XVII/Ne IX Heα we found that the parameter values log η (ergs cm^{-6}) > 50 and 7.26 $\leq$ log T_s (K) $\leq$ 7.7 are allowed. From our fits to the SSS and IPC data, the 90% confidence upper limit to the average temperature is log T = 6.925, which corresponds to a shock temperature of log T_s = 6.85 according to Hamilton & Sarazin (1984). This value is more than a factor of 2.6 lower than the minimum allowed shock temperatures from the HSC model for the FPCS data. We note that a similar high-temperature region of parameter space is allowed by the FPCS data alone using the single-temperature, single-time-scale NEI model. Relative enhancement of the O/Fe and Ne/Fe abundance ratios over their solar values brings the region of parameter space allowed by the FPCS data into agreement with the SSS/IPC data. Thus, although nearly solar abundances are consistent with the data in the HSC models, an enhancement in the abundances of O/Fe and Ne/Fe relative to solar values is suggested and would make the FPCS and SSS/IPC results consistent.

4. DISCUSSION

4.1. *Line Fluxes*

To compare fluxes predicted by the SSS/IPC model with those measured by the FPCS, it is necessary to correct the FPCS fluxes for the continuum. The FPCS is not well suited to determining the true continuum level since scans cover a relatively narrow range of energies which are rich in emission lines

[3] Our Fe XVII line corresponds to the Fe f line of HSC.

and blends. We did attempt to fit the continuum level in scans of clean, strong lines like O VIII Lyα, O VIII Lyβ, and Ne X Lyα. With relatively large errors, the fitted continuum fractions were consistent with the predictions of the best fit SSS/IPC model. When we correct the FPCS fluxes for the continuum fractions predicted by the model for the appropriate energy ranges, there is an overall difference of a factor of 2 between the SSS/IPC and the FPCS, with the SSS/IPC predictions being systematically lower than the FPCS observations. The O VIII Lyγ and Fe XVII lines, as noted above, are subject to systematic uncertainties in the FPCS efficiency. The remaining discrepancy must be attributed to other, unresolved systematic errors in the efficiencies of the instruments. We point out that the effect is roughly constant over the entire range of observations and that all the conclusions drawn from the FPCS data are based on taking ratios of line fluxes, and are consistent with the corresponding SSS/IPC results.

4.2. *Nucleosynthetic Models*

We compare our estimates for abundance ratios in N132D to the predictions of models for Type II supernova with progenitors of various masses. We use the abundances for O, Ne, Mg, Si, S, Ar, and Fe relative to each other from the SSS/IPC fits and the calculations of Thielemann et al. (1992) for the composition of the ejecta from Type II supernovae with 13, 15, 20, and 25 $M_\odot$ progenitors. Uncertainties in the calculated ejected masses were estimated by the authors to be approximately 30%. We assigned a larger error of 60% for the ejected mass of iron because there is additional uncertainty in the location of the mass cut in the iron core. The contribution from swept-up interstellar material behind the shock front is also included. Two cases for the abundances of the elements in the interstellar medium were considered: the mean elemental abundances of the LMC and solar metals that are underabundant by a single factor. In general, the LMC abundances (Russell & Dopita 1992) are 0.25–0.5 times their solar values, except for Mg and Si, which are anomalously high at 1.12 and 1.95 times solar, respectively (Table 2). These two measurements are based on observations of one or two lines in a few LMC supergiants, so we also consider solar abundances that are reduced by an overall factor for elements other than H and He.

For the remnants of each of the four progenitors, the total mass of a particular element is the sum of the ejected mass of that element from the supernova plus the mass of the swept-up interstellar medium weighted by the appropriate mass fraction. This calculated mass is proportional to the product of the elemental abundance in the remnant and the appropriate atomic weight. Because of this proportionality, we are effectively using ratios of the fitted elemental abundances. We fit the proportionality constant and the mass of the swept-up interstellar medium using the weighted orthogonal linear regression software ODRPACK (Boggs et al. 1990). Errors in both the calculated model mass and the observed abundances were included, as well as the errors in the LMC abundances. The resulting sum of squared deviations was assumed to be distributed like χ^2 for the appropriate number of degrees of freedom to assess the goodness of fit.

We considered models for which the swept-up interstellar mass in the remnant is between 100 and 500 $M_\odot$, which we believe is reasonable considering that a constant-density isothermal shell model for the HRI image suggests a remnant mass between 250 and 350 $M_\odot$ (Hughes 1987). We found that the models for remnants of all four progenitors were consistent with our data for either set of abundances with a probability for accepting the fit greater than 0.10.

The calculated O/Fe mass ratios for these models can be compared to the FPCS estimate for the remnant. The 13 $M_\odot$ model predicts ratios that are factors of 3–4 too low compared to the observed value, which implies that the mass cut of iron should be adjusted to eject 3–4 times more iron if the model correctly describes N132D. With an ejected iron mass of 0.24 $M_\odot$, this requires that over half of the 1.18 $M_\odot$ iron core remaining actually be ejected. Similarly, the 15 $M_\odot$ models predict ratios that are a factor of 2 too low compared to the observed value, implying that the mass cut of iron should be adjusted to eject twice as much iron. The O/Fe mass ratios of the 20 and 25 $M_\odot$ models are consistent with the observed values. Alternatively, if the mass cuts are correct, these results indicate that N132D is probably the remnant of a progenitor of mass $\sim 20\ M_\odot$.

5. CONCLUSIONS

Our analysis of spectral data from the *Einstein Observatory* supports indications from optical observations and preliminary X-ray studies that N132D is an ionizing, oxygen-rich remnant. As such, it is appropriately placed in the class of remnants including Cassiopeia A and Puppis A in our own Galaxy. These remnants are conjectured to be the aftermath of Type II explosions in massive ($>12\ M_\odot$) stars, which synthesize the oxygen during their normal evolution.

Spectral fits of data from the Solid State Spectrometer (SSS) and Imaging Proportional Counter (IPC) to a single-temperature, single-ionization time-scale nonequilibrium ionization model yields a temperature of 8.4×10^6 K and an ionization age of 6.1×10^3 cm^{-3} yr. Measured flux ratios from the Focal Plane Crystal Spectrometer (FPCS) constrain the temperature and ionization age jointly to values that are consistent with the SSS/IPC fits. The two data sets indicate an overabundance of oxygen relative to iron by a factor of at least 1.9 compared to the solar value and an abundance of neon relative to oxygen that is approximately 0.5–1.0 times the solar value. Abundance information from the SSS/IPC fits is compared to the composition of ejecta for Type II supernova explosions of 13, 15, 20, and 25 $M_\odot$ stars including a contribution from swept-up interstellar material behind the shock front. Models for remnants of all four progenitors are consistent with our data with a probability for accepting the fits greater than 0.10, provided that the lower mass remnants eject a large fraction of their iron cores.

A Sedov model of the remnant as calculated by Hamilton et al. (1983) accommodates FPCS line flux ratios of O, Ne, and Fe without an adjustment of elemental abundances but requires shock temperature higher than we observe with the SSS and IPC. Enhancement of oxygen and neon relative to iron lowers the shock temperature into consistency with the SSS/IPC result and is consistent with results from other aspects of our analysis.

Several people contributed to the observation planning and early analysis of N132D. We thank P. F. Winkler, C. Berg and T. Pfafman, and K. Flanagan. K. Lum made significant contributions to the recent data analysis. This work was supported in part by NASA grants NAG8-494, NAS8-36748, and NAG8-670 (JPH) as well as Smithsonian Institution funds.

REFERENCES

Allen, C. W. 1973, Astrophysical Quantities (London: Athlone), 30
Bhatia, A. K., Fawcett, B. C., Lemen, J. R., Mason, H. E., & Phillips, K. J. H. 1989, MNRAS, 240, 421
Boggs, P. T., Donaldson, J. R., Byrd, R. H., & Schnabel, R. B. 1990, ACM Trans. Math. Soft., 15, 348
Canizares, C. R. 1985, X-Ray Astronomy '84, ed. M. Oda & R. Giacconi (Tokyo: SAS), 275
———. 1990a, IAU Colloq. 115, High Resolution X-Ray Spectroscopy of Cosmic Plasmas, ed. P. Gorenstein & M. Zombeck (Cambridge: Cambridge Univ. Press), 136
———. 1990b, NATO Advanced Research Workshop, Physical Processes in Hot Cosmic Plasmas, ed. W. Brinkmann, A. C. Fabian, & F. Giovannelli (Dordrecht: Reidel), 17
Canizares, C. R., Clark, G. W., Markert, T. H., Berg, C., Smedira, M., Bardas, D., Schnopper, H. W., & Kalata, K. 1979, ApJ, 234, L33
Canizares, C. R., Winkler, P. F., Markert, T. H., & Berg, C. 1983, IAU Symp. 101, Supernova Remnants and Their X-Ray Emission, ed. J. Danziger & P. Gorenstein (Dordrecht: Reidel), 205
Christian, D. J. 1992, Ph.D. thesis, Univ. Maryland
Clark, D. H., Tuohy, I. R., Long, K. S., Szymkowiak, A. E., Dopita, M. A., Mathewson, D. S., & Culhane, J. L. 1982, ApJ, 255, 440
Danziger, I. J., & Dennefeld, M. 1976, ApJ, 207, 394
Giacconi, R., et al. 1979, ApJ, 230, 540
Gorenstein, P., Harnden, R., & Tucker, W. 1974, ApJ, 192, 661
Gronenschild, E. H. B. M., & Mewe, R. 1982, A&AS, 48, 305
Hamilton, A. J. S., & Sarazin, C. L. 1984, ApJ, 281, 682
Hamilton, A. J. S., Sarazin, C. L., & Chevalier, R. A. 1983, ApJS, 51, 115 (HSC)
Holt, S. S., White, N. E., Becker, R. H., Boldt, E. A., Mushotzky, R. F., Serlemitsos, P. J., & Smith, B. W. 1979, ApJ, 234, L65
Hughes, J. P. 1987, ApJ, 314, 103
Hughes, J. P., & Helfand, D. J. 1985, ApJ, 291, 544
Itoh, H. 1977, PASJ, 29, 813
Lasker, B. M. 1978, ApJ, 223, 109
———. 1980, ApJ, 237, 765
Long, K. S., Helfand, D. J., & Grabelsky, D. A. 1981, ApJ, 248, 925
Markert, T. H., Canizares, C. R., Pfafman, T., Vedder, P., Winkler, P. F., & Pradhan, A. 1984, IAU Colloq. 86, Ultraviolet and X-Ray Spectroscopy of Astrophysical and Laboratory Plasmas, ed. G. A. Doschek (Washington: Naval Research Lab), 76
McKenzie, D. L., Landecker, P. B., Broussard, R. M., Rugge, H. R., Young, R. M., Feldman, U., & Doschek, G. A. 1980, ApJ, 241, 409
Mewe, R., & Gronenschild, E. H. B. M. 1981, A&AS, 45, 11
Mewe, R., Gronenschild, E. H. B. M., & van den Oord, G. H. J. 1985, A&AS, 62, 197
Morrison, R., & McCammon, D. 1983, ApJ, 270, 119
Nugent, J. J. 1984, Ph.D. thesis, California Institute of Technology
Panagia, N., Gilmozzi, R., Machetto, F., Adorf, H.-M., & Kirshner, R. P. 1991, ApJ, 350, L23
Pradhan, A. 1982, ApJ, 263, 477
Raymond, J. C., & Smith, B. W. 1977, ApJS, 35, 419
Russell, S. C., & Dopita, M. A. 1992, ApJ, 384, 508
Schattenburg, M. L., & Canizares, C. R. 1986, ApJ, 301, 759
Sedov, L. I. 1959, Similarity and Dimensional Methods in Mechanics (New York: Academic)
Shull, J. M. 1982, ApJ, 262, 308
Thielemann, F.-K., Nomoto, K., Shigeyama, T., Tsujimoto, T., & Hashimoto, M. 1992, 31st Herstmonceaux Conference, Elements and the Cosmos, ed. R. J. Terlevich (Cambridge: Cambridge Univ. Press), 609
Vedder, P. W., Canizares, C. R., Clark, G. W., Markert, T. H., & Pradhan, A. 1986, ApJ, 307, 269
Westerlund, B. E., & Mathewson, D. S. 1966, MNRAS, 131, 371
Winkler, P. F., Canizres, C. R., & Bromley, B. C. 1983, IAU Symp. 101, Supernova Remnants and Their X-Ray Emission, ed. J. Danziger & P. Gorenstein (Dordrecht: Reidel), 245